Applied Catalysis B: Environmental 317 (2022) 121681

Contents lists available at ScienceDirect

Applied Catalysis B: Environmental

journal homepage: www.elsevier.com/locate/apcatb

Efficient electrocatalytic conversion of CO_2 to ethanol enabled by imidazolium-functionalized ionomer confined molybdenum phosphide

Mohammadreza Esmaeilirad [a], Alireza Kondori [a], Nannan Shan [b], Mahmoud Tamadoni Saray [c], Sreya Sarkar [c], Ahmad M. Harzandi [a], Constantine M. Megaridis [c], Reza Shahbazian-Yassar [c], Larry A. Curtiss [b], Carlo U. Segre [d], Mohammad Asadi [a,*]

[a] Department of Chemical and Biological Engineering, Illinois Institute of Technology, Chicago, IL 60616, USA
[b] Materials Science Division, Argonne National Laboratory, Argonne, IL 60439, USA
[c] Department of Mechanical and Industrial Engineering, University of Illinois at Chicago, Chicago, IL 60607, USA
[d] Department of Physics & CSRRI, Illinois Institute of Technology, Chicago, IL 60616, USA

ARTICLE INFO

Keywords:
CO_2 reduction reaction
Transition metal phosphides
Imidazolium
in-situ Raman
Ethanol electrosynthesis

ABSTRACT

An effective electrochemical carbon dioxide reduction reaction (eCO_2RR) requires the discovery of a catalytic system that is highly active and selective for multi-carbon products together with superior CO_2 diffusion at a catalyst layer to minimize the reduction barriers. Here, we found a catalytic system that uses molybdenum phosphide (MoP) nanoparticles covered by imidazolium-functionalized ionomer (Im) that promotes CO_2 diffusion at the catalyst layer toward the catalyst surface, where CO_2 is reduced to ethanol (C_2H_5OH). The electrochemical results with the MoP-Im co-catalyst show a C_2H_5OH production Faradaic efficiency and a cathodic energy efficiency of 77.4% and 63.3%, respectively, at a potential as low as − 200 mV *vs.* RHE. The electrochemical experiments along with our physicochemical characterizations indicate that the Im improves CO_2 diffusion and balances water content resulting in a higher CO_2-to-water ratio at the catalyst layer and fine-tunes the electronic properties of Mo atoms at the MoP surface. *In-situ* Raman spectroscopy reveals that a high number of adsorbed *CO intermediates on the surface and a higher binding strength of *CO intermediates on the Mo surface sites in the presence of imidazolium molecules are the main reasons for a superior C-C coupling and thereby the improved C_2H_5OH formation.

1. Introduction

The US economy accounts for the release of a large amount of carbon dioxide (CO_2) into the atmosphere, causing severe environmental impacts [1]. However, CO_2 can be directly converted to value-added products via an electrochemical process driven by renewable energy that provides a promising path to carbon-neutral manufacturing of chemicals and fuels at the gigaton scale [2,3]. While recent studies have mainly focused on the development of catalysts to effectively produce multi-carbon (C_2^+) products, it is also important to improve CO_2 diffusion (mass transport) to the catalyst surface where CO_2 is adsorbed and then converted to $*CO_2^-$ intermediates that are identified to be thermodynamically uphill steps in many catalytic systems leading to a high overpotential and therefore, a low energy efficiency of the electrocatalytic CO_2 reduction reaction (eCO_2RR) [4,5]. This requires the discovery of a novel catalytic system that has a dual effect: (i) high activity and selectivity toward C_2^+ products, and (ii) high CO_2 affinity to reduce diffusion limitations of the reaction. Recent studies have found that imidazolium-based ionic liquids can improve eCO_2RR performance by lowering the thermodynamic barriers of the reaction [4,6,7]. The imidazolium cations can also enhance the diffusion of CO_2 to the catalyst surface and balance the water content needed for the reaction [8].

In the quest for catalysts to produce C_2^+ chemicals in eCO_2RR, transition metal phosphide (TMPs) have received great attention due to their low overpotentials and high selectivity toward C_2^+ products, such as 2,3-furandiol ($C_4H_4O_3$) [9], methylglyoxal ($C_3H_4O_2$) [10], and ethanol (C_2H_5OH) [11,12]. It has been shown that nanostructured TMPs have a promising catalytic ability owing to their unique structural properties that provide a high density of metal active sites at the surface with outstanding electronic properties, *i.e.*, high density of d-orbital electrons

* Corresponding author.
E-mail address: m.asadi@iit.edu (M. Asadi).

https://doi.org/10.1016/j.apcatb.2022.121681
Received 23 March 2022; Received in revised form 24 June 2022; Accepted 26 June 2022
Available online 30 June 2022

at the Fermi energy and low work function that can be ideal for electrocatalysis [13].

In this study, we have demonstrated a novel catalytic system with molybdenum phosphide (MoP) nanoparticles, a TMP, as the catalyst, and an imidazolium-functionalized ionomer (Im) as a catalyst helper that works remarkably well as a unified system to effectively produce C_2H_5OH in a hybrid electrolyte of 3 M potassium hydroxide (KOH) and 3 M potassium chloride (KCl).

2. Experimental section

2.1. Synthesis of MoP-Im and MoP catalysts and the ionomer

Ammonium molybdate tetrahydrate ($(NH_4)_6Mo_7O_{24}.4\ H_2O$, Sigma Aldrich), ammonium hydrogen phosphate ($(NH_4)_2HPO_4$, Sigma Aldrich) and citric acid ($C_6H_8O_7$, Sigma Aldrich) were used to synthesize MoP nanoparticles. First, $(NH_4)_6Mo_7O_{24}.4\ H_2O$ (4.68 g) and $(NH_4)_2HPO_4$ (0.5 g) with a molar ratio of 1:1 were dissolved in a sufficient amount of DI-water (40 ml) at 90 ºC for 2 h. Then citric acid (0.1 g) was added to the solution in a molar ratio of 2 (citric acid): 1 (Mo). After we evaporated the excess water, the remaining brown slurry was dried in vacuum at 120 ºC for 24 h and hand ground to get the MoP precursor. The precursor was then sintered at 500 ºC for 5 h under nitrogen flow. The obtained dark gray powder was then heated to 650 ºC at a heating rate of 10 ºC/min and kept at 650 ºC for 2 h under a controlled flow of 8 vol% of hydrogen/argon to obtain the MoP nanoparticles. The as-synthesized MoP nanoparticles were then deactivated under mixed 2 vol% oxygen/argon flow for 2 h, after which they could be handled in ambient air [13]

The Im used for our MoP-Im was synthesized by mixing 2.4 g of divinylbenzene ($C_6H_4(CH{=}CH_2)_2$, Sigma Aldrich), 0.048 g of cyclohexane carbonitrile ($C_6H_{11}CN$, Sigma Aldrich), 0.08 g 1,1-azobis cyclohexane carbonitrile ($NCC_6H_{10}N = NC_6H_{10}CN$, Sigma Aldrich) and 1.5 g of 2-methylimidazole ($C_4H_6N_2$, Sigma Aldrich) in 10 ml of dimethylformamide ($HCON(CH_3)_2$, Sigma Aldrich). The mixture then was heated to 80 ºC for 9 h to obtain a white solid, the ionomer precursor. Next, the precursor was washed with 15 ml of dichloromethane (CH_2Cl_2, Sigma Aldrich) to remove residual dimethylformamide solvent and excess reagents. The synthesized ionomer was dried in a vacuum oven at 50 ºC to remove any residual impurities [14,15].

To prepare the MoP-Im matrix, 0.1 g of MoP nanoparticles was dispersed in 15 ml of isopropyl alcohol (C_3H_7OH, Sigma Aldrich). Then synthesized Im was added to the solution and mixed with MoP nanoparticles for 2 h at 50 ºC to obtain MoP-Im ink with 8 wt% of the Im.

2.2. Electrochemical CO_2 reduction reaction setup

A two-compartment three-electrode flow electrolyzer was used for electrochemical experiments. It consists of housings, gaskets, anode and cathode flow-field plates, and an anion exchange membrane. The anode and cathode housings (10 × 10 × 1 cm) were made from stainless steel and serve to deliver liquid and gas feeds to the anode and cathode parts, through 0.125" NPT ports with barbed tubing adapters. The cathode and anode housings with active surface areas of 5 cm^2 sandwich an ionic exchange membrane (Sustainion X37–50 Grade RT, Dioxide Materials). The membrane was treated in a CO_2 saturated 3 M potassium hydroxide solution for 12 hr at 50 °C prior to use. A peristaltic pump (Masterflex, Cole-Parmer) was used to continuously pump a hybrid 3 M potassium hydroxide and 3 M potassium chloride electrolyte with flow rate of 30 ml/min through the cathode and anode sides. A mass flow controller (SmartTrak 50, Sierra, calibrated with CO_2 gas) connected to the humidifier kit, was used to set the flow rate of CO_2 at 30 ml/min. Iridium oxide (IrO_2) powder (Sigma Aldrich) and Ag/AgCl (saturated KCl) were employed as anode and reference electrodes, respectively. More details about electrochemical setup and experiments can be found in the Supplementary Materials section S8.

2.3. Product characterization and energy conversion efficiency measurement

The products of electrochemical CO_2RR were detected and quantified using a gas chromatograph (GC, SRI 8610 C Multiple Gas Analyzer), differential electrochemical mass spectroscopy (DEMS, HPR-40, Hiden Analytical) and nuclear magnetic resonance spectroscopy (NMR, 500 MHz Bruker Advance III HD). The GC system comprised a sampling loop equipped with a flame ionization detector (FID) and a thermal conductivity detector (TCD). Ultra-high purity helium (He) and nitrogen (N_2) (UHP 99.99%, Airgas) were used as the carrier gases to identify any possible type of product. The column oven was maintained at 40 ºC for 2 min followed by a temperature ramp at 20 ºC/min to 250 ºC which was held constant for 1 min for a precise product analysis. Moreover, the *in-situ* DEMS was used to validate the obtained products from the GC system by continuously detecting all possible products, even at trace amounts (partial pressure of 1 $\times 10^{-13}$ Torr), during the experiments, resulting in a more precise measurement. The signal responses of the DEMS instrument for different products were calibrated by feeding standard samples into the mass spectrometer. An electron energy of 70 eV was used for ionization of all species, with an emission current of 500 μA. All mass-selected product cations were detected by a secondary electron multiplier with a detector voltage of 1200 V for maximizing the signal to noise ratio of the products. The NMR spectroscopy was employed to characterize the liquid phase products. To do so, 0.5 ml of the electrolyte was taken and mixed with 0.2 ml Deutrium oxide (D_2O 99.9% deuterium, Sigma-Aldrich) in 5 mm NMR glass tube (Wilmad®). All NMR spectra were collected using a 500 MHz Bruker Advance III HD system equipped with a TXO Prodigy probe with Z-gradient for enhanced sensitivity at 298 K. More details about the products analyses of electrochemical CO_2RR can be found in Supplementary Materials section S9.

The C_2H_5OH energy conversion efficiency is calculated based on experimental measurements of the cathodic half-cell reaction. The overpotential for the anodic water splitting reaction ($O_2 + 4\ H^+ + 4e^- \leftrightarrow 2\ H_2O$, $E^o_{\text{water splitting}} \cong 1.23$ V vs RHE) is assumed to be zero. The C_2H_5OH energy conversion efficiency for MoP-Im catalyst obtained using Eq. (1):

$$\text{Cathodic Energy Efficiency}(\%) = \frac{E^0_{ethanol} \times FE_{\text{ethanol}}}{E_{\text{full cell}}} \quad (1)$$

Where $E_{\text{full cell}}$ is a summation of the cathodic half-cell potential obtained in the experiments with thermodynamic potential of the anodic water splitting reaction where no overpotential losses at the anode is considered ($E_{\text{full cell}} = E_{\text{cathode}} - 1.23$). $E^0_{ethanol}$ is thermodynamical potential of C_2H_5OH production that is calculated to be $E^0_{ethanol} \cong -1.15$ V using the Gibbs free energy of species by using $\Delta G = -nFE$.

2.4. Electrochemical impedance spectroscopy (EIS) and CO_2 diffusion coefficient calculations

EIS experiments were employed to compare the CO2 diffusion coefficient for MoP-Im and MoP catalytic systems under an identical experimental condition.

At high overpotentials where both diffusion and kinetic processes are involved in the reaction, the overall resistance is a summation of R_{ct} charge transfer resistance (kinetic parameter observed at high frequency region) and Z_R (real component of Z_ω shown in Fig. S18) that shows frequency-dependent resistance in Warburg impedance (diffusion parameter observed at low frequency region). The EIS experiments were conducted under identical experimental condition at a potential of − 0.4 V for both MoP-Im and MoP catalytic systems. At this potential, the reaction rate, current density, is overwhelmingly limited by the diffusion of CO_2 reactants to the surface of catalyst (diffusion-controlled region).

The Nyquist plots for different catalysts were recorded over a fre-

quency range of 1–2 × 10^5 Hz. The CO_2 diffusion coefficient at low frequency range (< 10 Hz) for the MoP-Im and MoP catalysts are obtained using Eq. (2):

$$D = \frac{R^2T^2}{2A^2n^4F^4C^2\sigma_w^2} \quad (2)$$

Where D is the CO_2 diffusion coefficient, R is the universal gas constant, T is the temperature, A is the electrode area, n is the number of transferred electrons, F is Faraday's constant, and C is the concentration of the oxidants. More details about EIS experiments and CO_2 diffusion coefficient calculations can be found in Supplementary Materials section S14.

2.5. In-situ electrochemical Raman spectroscopy

The *in-situ* electrochemical Raman spectroscopy was conducted in a custom designed electrochemical cell employing Horiba LabRAM HR Evo Confocal Raman (Horiba scientific instrument, US). A 532 nm laser source, a HORIBA Synapse detector, 600 g/mm grating and a long-distance 50x objective was used to probe the samples. The measurement parameters such as acquisition time, averaging parameters and laser power were all optimized to enhance the signal to noise ratio of the spectra. The Raman laser was focused onto the surface of the working electrode through a transparent quartz window (1 mm thick) and a thin layer of electrolyte with a total optical path of 3.25 mm. More details about *In-situ* Raman spectroscopy can be found in Supplementary Materials section S17.

2.6. Theoretical study

The density functional theory (DFT) calculations were conducted with the commercial code VASP. The exchange-correlation energies were obtained with GGA-PBE functional. The van der Waals corrections were obtained with zero damping DFT-D3 method of Grimme. The cut-off energies for slab models were set to 400 eV and a k-point mesh of 3 × 3 × 1 in Monkhorst-pack scheme were used. The self-consistent iterations were stopped until the force is less than 0.02 eV/Å. All calculations included the dipole corrections. More details of computational methods can be found in the Supplementary Materials section S18.

3. Results and discussion

3.1. Characterization of structure and morphology

To gain an understanding of structural, physicochemical, and electronic properties of synthesized catalysts, *i.e.*, MoP-Im and MoP, and identify the key factors that affect their electrocatalytic properties, we have performed different molecular and atomic scale characterizations, such as X-ray diffraction (XRD), scanning electron microscopy (SEM), X-ray photoelectron spectroscopy (XPS), X-ray absorption fine structure (XAFS), and high-resolution transmission electron microscopy (HRTEM), (sections S3-S7, Supplementary Materials).

The XRD experiment was employed to study the lattice structure of the MoP-Im and MoP catalysts (section S3, Supplementary Materials). The XRD patterns of both MoP-Im and MoP show a sharp peak at 2θ= 43.4° along with three pronounced peaks at 2θ= 32.4°, 57.5°, and 28.3° corresponding to (101), (100), (110) and (001) crystal surfaces of

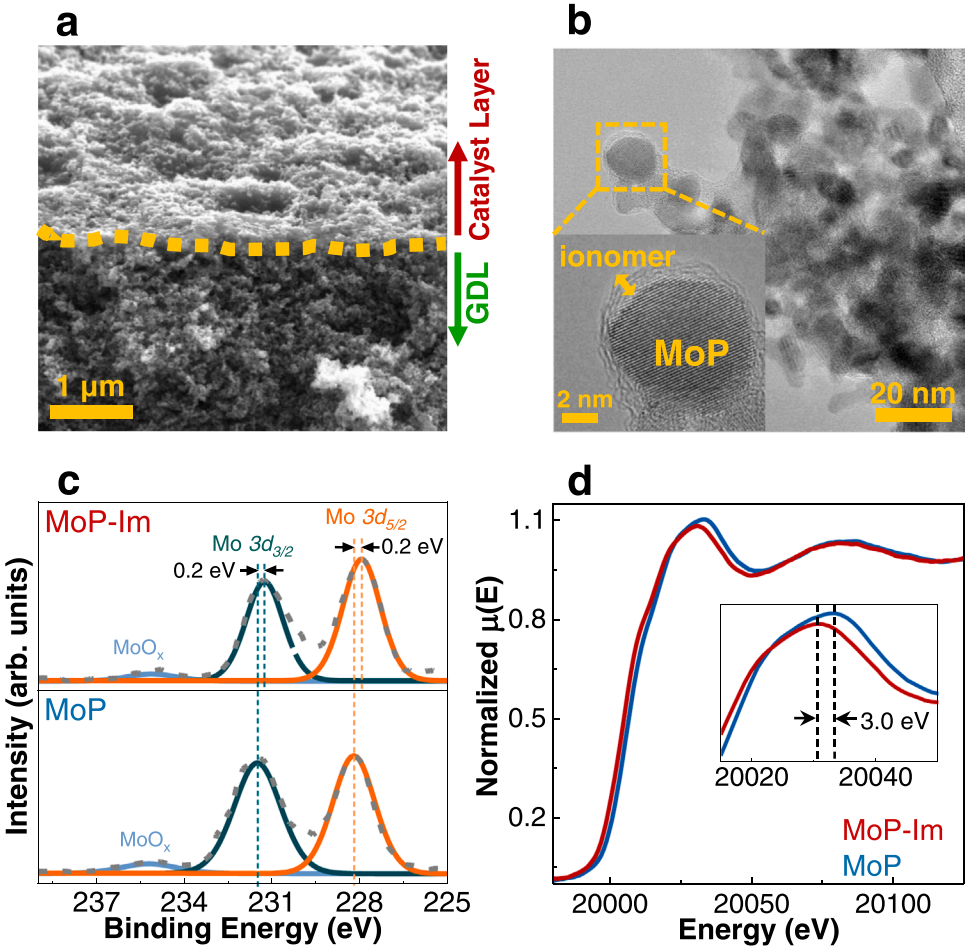

Fig. 1. Structural and physicochemical characterizations of studied catalysts. (a) Cross-sectional scanning electron microscopy (SEM) image of MoP-Im electrode. The electrode was prepared by coating the MoP-Im catalyst on a gas diffusion layer (GDL). **(b)** High-resolution transmission electron microscopy (HRTEM) image of MoP-Im catalyst. The inset shows a laminar conformal overcoating of the ionomer. **(c)** Mo 3d high-resolution X-ray photoelectron spectroscopy (XPS) spectra of MoP-Im and MoP. **(d)** X-ray absorption near edge structure (XANES) spectra of MoP-Im compared to MoP.

MoP, respectively (Fig. S3, Supplementary Materials) [13]. The XRD patterns of MoP-Im and MoP shown in Fig. S3 indicate all Bragg peaks of MoP, verifying their homogeneous and pure structures. The XRD results also exhibit a hexagonal $P\bar{6}m2$ space group for both MoP-Im and MoP catalyst, where the length of all Mo-P bonds are 2.46 Å suggesting no structural changes due to the ionomer coating.[16].

The cross-sectional and surface morphologies of the MoP-Im coated on the GDL are shown in Figs. 1a and S4a (section S4, Supplementary Materials). The cross-sectional SEM image of the MoP-Im deposited on GDL further shows the morphology of the catalyst layer with a thickness of 2–3 μm. We also performed energy dispersive X-ray (EDX) spectroscopy analysis shown in Fig. S4a to study the elemental distribution of Mo, P, N, and C atoms present in the MoP-Im electrode (section S4, Supplementary Materials). Our EDX analysis indicates a homogenous distribution of Mo and P atoms from MoP as well as N and C atoms from the Im with an approximate thickness of 2–3 μm at the top of the cross-sectional SEM image.

HRTEM experiments were performed to further characterize particle shape, size, and thickness of ionomer in the synthesized MoP-Im (section S5, Supplementary Materials). Fig. 1b shows the image of the well-dispersed MoP-Im, confirming its spherical shape and uniform size distribution. Fig. S5 indicates a high-magnification HRTEM image of a single MoP-Im particle confirming the presence of a continuous and conformal ionomer layer with a thickness of less than 2 nm, on the surface of MoP nanoparticles with an average particle size of 8–10 nm (section S5, Supplementary Materials). Our Atomic resolution ABF image of the < 001 > zone axis is also shown in Fig. S5c and d with corresponding Fast Fourier transform (FFT) image in the inset confirming a hexagonal structure of MoP crystal in both MoP-Im and MoP catalysts. The crystal model in the < 001 > zone axis is overlaid on Fig. S5c (section S5, Supplementary Materials). Fig. S5d shows the image simulation using the crystal model at the same zone axis. The good match among model, experiment, and simulated images confirms the hexagonal geometry of MoP crystal with dominant Mo atoms at the surface, which are the potential active sites in eCO_2RR.

The XPS experiments were performed to analyze the surface chemistry of MoP-Im in comparison with MoP nanoparticles (section S6, Supplementary Materials). Fig. 1c depicts the Mo 3*d* XPS spectra of MoP-Im, indicating two intense peaks centered at 228.36 and 231.7 eV attributed to Mo $3d_{5/2}$ and Mo $3d_{3/2}$ of Mo^{+3} atoms in MoP-Im.[17] These results show about 0.2 eV shifts in the Mo $3d_{5/2}$ and Mo $3d_{3/2}$ peaks of MoP-Im compared to the MoP indicating that the ionomer coating layer alters the electronic properties of Mo atoms in MoP. The P 2*p* XPS spectra of MoP-Im and MoP are shown in Fig. S6a (section S6, Supplementary Materials). The results indicate spin-orbit split 2*p* peaks of $2p_{3/2}$ at a binding energy of 130.7 eV and $2p_{1/2}$ at a binding energy of 131.6 eV. The peaks are attributed to the Mo-P bond [17], suggesting an oxidation state of − 3 for P atoms for both MoP-Im and MoP catalysts (section S6, Supplementary Materials).[13] Furthermore, the N 1 *s* XPS spectra of MoP-Im shown in Fig. S6b indicate two distinct peaks centered at binding energies of 397.3 and 400.5 eV corresponding to nitrogen atoms (=N- and –N < , respectively) of imidazolium (section S6, Supplementary Materials) [18]. In contrast, the XPS spectrum of bare MoP does not show any N 1 *s* peak, confirming the existence of the ionomer coating layer for MoP-Im. This is further confirmed by XPS depth profiling analysis that suggests the surface of MoP-Im is dominated by the ionomer (Fig. S7, Supplementary Materials).

Next, we carried out *ex-situ* X-ray absorption spectroscopy (XAS) measurements at the Mo K-edge on MoP-Im and MoP catalysts to determine the effect of the Im on the electronic structure and local geometry of the MoP-Im (section S7, Supplementary Materials). Comparing X-ray absorption near edge structure (XANES) spectra of MoP-Im and MoP catalysts shown in Fig. 1d indicate that the white line in MoP-Im shifts to lower energy (3.0 eV) compared to that of MoP, whereas the peak height remains almost the same [19]. This result suggests that the Mo atoms on the surface of MoP-Im catalyst are slightly reduced compared to Mo atoms on the surface of MoP catalyst (sections S6 and S7, Supplementary Materials).[20] The Fourier transforms of extended X-ray absorption fine structure (EXAFS) results also indicate that Mo-P bond distances for the studied catalysts are virtually identical, confirming no structural changes for MoP-Im compared to MoP nanoparticles (see Table S1 and Fig. S8, Supplementary Materials).

3.2. Electrochemical characterization

We tested the eCO_2RR performances of synthesized MoP-Im and MoP catalysts in a custom-designed three-electrode electrochemical cell (section S8, Supplementary Materials). All electrochemical tests in this study were carefully conducted under identical experimental conditions using a hybrid 3 M KOH and 3 M KCl electrolyte. This combination was selected because it suppresses hydrogen production and increases hydrogenation processes in eCO_2RR.[21,22] We evaluated the overall activities of MoP-Im and compared with MoP by performing linear sweep voltammetry (LSV) experiments in the potential range of 0 to − 0.5 V versus reversible hydrogen electrode (*vs.* RHE, all potentials are reported with respect to RHE in this study) with a scan rate of 20 mV/s (Fig. 2a). As shown in Fig. 2a, MoP-Im co-catalyst indicates a current density of − 90.8 mA/cm^2 at the potential of − 0.5 V that is about 1.4 times higher than that of MoP nanoparticles (−63.8 mA/cm^2 at −0.5 V), indicating higher overall activity of the MoP-Im co-catalyst system compared to MoP nanoparticles.

We also measured the selectivity of synthesized MoP-Im and MoP catalysts by performing chronoamperometry experiments (CA) at different potentials (section S9, Supplementary Materials). The product streams were analyzed using gas chromatography (GC), differential electrochemical mass spectrometry (DEMS), and nuclear magnetic resonance spectroscopy (NMR). Our measurements indicate that the MoP-Im starts to produce C_2H_5OH at a potential of − 0.2 V (that is equivalent to 280 mV overpotential considering C_2H_5OH thermodynamic potential of +0.08 V) with a maximum FE of 77.4% (Table S2, Supplementary Materials). On the other hand, MoP is mainly selective for methanol (CH_3OH) production with a maximum FE of 60.8% and C_2H_5OH formation FE of 21.8%, at the same potential (Table S2, Supplementary Materials). Moreover, the product selectivity analyses reveal that the MoP-Im and MoP catalysts produce other eCO_2RR products, such as carbon monoxide (CO), methane (CH_4), and ethylene (C_2H_4) at the potential of − 0.2 V (section S9, Supplementary Materials). Isotope ^{13}C CO_2 experiments confirm that the CO_2 gas present inside the electrolyte is the only source of the formed products for MoP-Im in the eCO_2RR (section S10, Supplementary Materials).

We calculated partial current densities of different products considering the total current densities and FEs of MoP-Im and MoP catalysts (Fig. 2b, and Fig. S11, Supplementary Materials). Fig. 2b indicates that using the MoP-Im catalyst, the C_2H_5OH formation starts at a potential of − 0.2 V with a current density of − 8.6 mA/cm^2 and reaches its maximum of − 54.9 mA/cm^2 at a potential of − 0.5 V. The maximum C_2H_5OH formation current density of MoP-Im co-catalyst (−54.9 mA/cm^2 at −0.5 V) is about 5 times higher than that of MoP (−10.7 mA/cm^2 at −0.5 V) indicating higher C_2H_5OH formation activity of MoP-Im compared to MoP. Furthermore, at the potential of − 0.5 V, MoP-Im catalyst produces other eCO_2RR products such as CH_3OH, C_2H_4, CH_4, and CO with partial current densities of − 8.3, − 5, − 3.3, and − 7.3 mA/cm^2, respectively.

We benchmarked the MoP-Im and MoP catalysts by comparing their C_2H_5OH formation energy efficiencies to state-of-the-art electrocatalysts in the literature at their highest C_2H_5OH formation FE considering no anodic overpotential losses (Fig. 2c, and Table S4, Supplementary Materials). Fig. 2c indicates C_2H_5OH formation cathodic energy efficiency (cathodic EE_{C2H5OH}) of 63.3% and 17.9% for MoP-Im and MoP catalysts, respectively. As shown in this figure, the cathodic EE_{C2H5OH} of MoP-Im is about 1.2 and 2-times higher than that of recently studied Cu/C (55.2%)

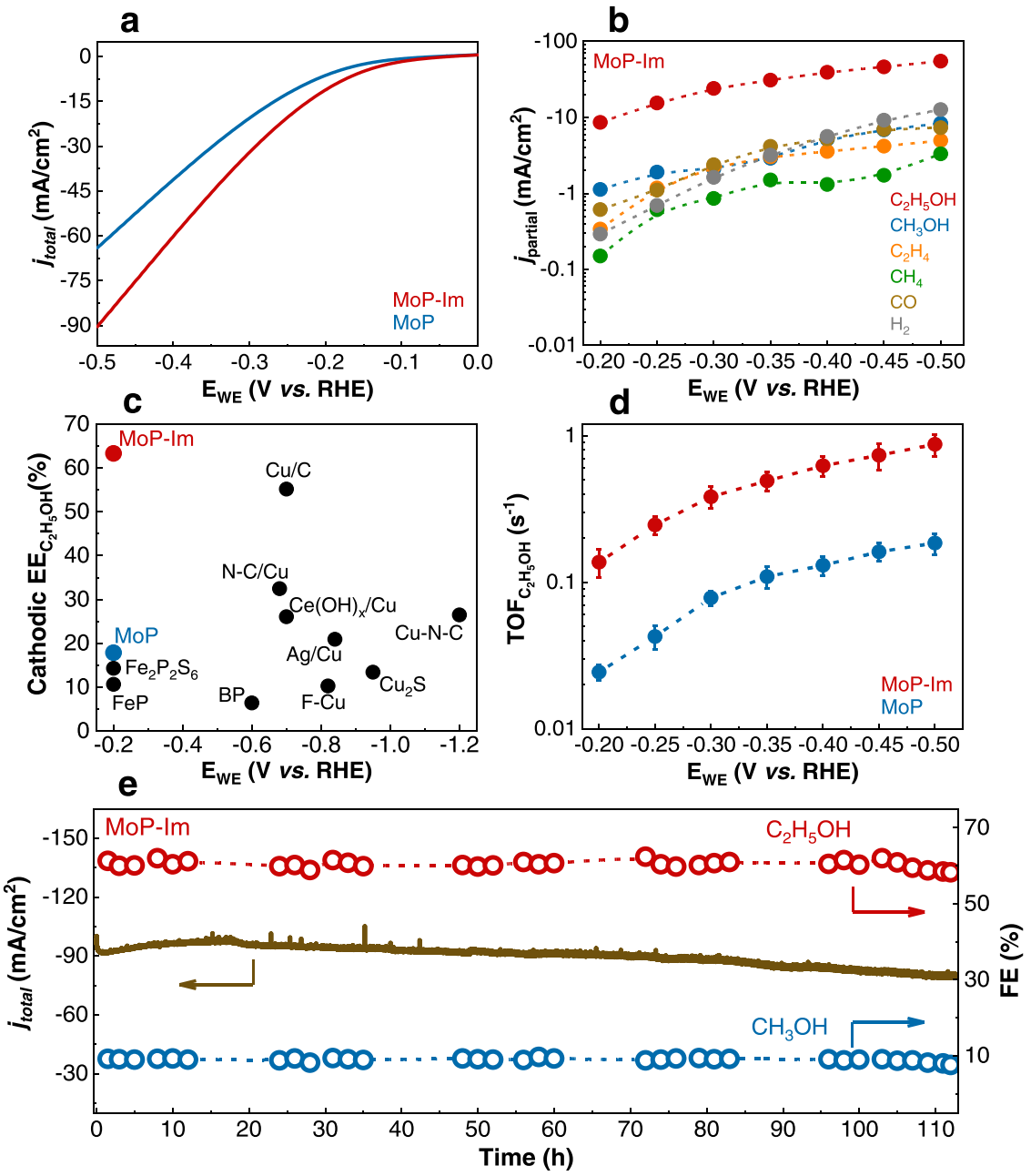

Fig. 2. Electrocatalytic performance of MoP-Im and MoP for eCO_2RR in a two-compartment three-electrode electrochemical cell using a hybrid 3 M KOH and 3 M KCl electrolyte. (a) Linear sweep voltammetry (LSV) results of MoP and MoP-Im in a potential range of 0 to − 0.5 V. (b) Partial current densities of different products for MoP-Im catalyst as a function of potentials. (c) Cathodic energy efficiency for C_2H_5OH formation (Cathodic EE_{C2H5OH}) of MoP-Im and MoP compared to state-of-the-art catalytic systems.[11,12,23,24–30] The data shown in this figure are obtained at the maximum C_2H_5OH formation FE of each catalyst in the literature considering no overpotential losses at the anode. (d) C_2H_5OH formation turnover frequency (TOF_{C2H5OH}) calculations for MoP and MoP-Im. (e) Stability analysis of MoP-Im in eCO_2RR at a potential of − 0.5 V. This figure shows the overall current density of MoP-Im as a function of time. Ethanol and methanol production FEs are also represented over time.

[24] and N-C/Cu (32.5%)[25] catalytic systems, respectively.

To understand the actual per atom activity of the MoP-Im co-catalyst, we measured C_2H_5OH formation turnover frequencies (TOF_{C2H5OH}) of MoP-Im and MoP catalysts where TOF_{C2H5OH} values were normalized to the number of Mo atoms identified as the potential active sites at the surface by our characterization analyses (section S11, Supplementary Materials) [22]. Fig. 2d shows the calculated TOF_{C2H5OH} of MoP-Im and MoP catalysts in the potential range of − 0.2 to − 0.5 V. The results indicate a TOF_{C2H5OH} of 0.137 s^{-1} at a potential of − 0.2 V for the MoP-Im, that is about 5.7 times higher than MoP (0.024 s^{-1} at −0.2 V). Fig. 2d exhibits that the TOF_{C2H5OH} values for both MoP-Im and MoP catalysts increase gradually with increasing potential. Moreover, MoP-Im shows a maximum TOF_{C2H5OH} of 0.875 s^{-1} at the potential of − 0.5 V, whereas the TOF_{C2H5OH} for MoP is 0.185 s^{-1}. Since TOF values represent the intrinsic activity of catalytically active sites (*i.e.*, Mo atoms), the difference in TOF_{C2H5OH} values at the same applied potentials for MoP-Im and MoP catalysts is potentially due to the presence of the ionomer in the MoP-Im co-catalyst [24].

To realize the C_2H_5OH formation kinetic parameters of the MoP-Im and MoP catalysts, we employed Tafel plot analysis using the potentials and partial C_2H_5OH current densities. Our analysis, shown in Fig. S16 (section S12, Supplementary Materials), indicates nearly the

same C_2H_5OH Tafel slopes for MoP-Im and MoP catalysts suggesting a similar reaction mechanism for both catalytic systems. However, the MoP-Im co-catalyst has a C_2H_5OH exchange current density ($i_{o,C2H5OH}$) of 325 μA that is 5.6-fold higher than that of MoP (58 μA). This result clearly shows a higher intrinsic catalytic activity of Mo atoms in MoP-Im compared with MoP for production of C_2H_5OH [31].

The stability of the MoP-Im was studied by performing a long-term eCO_2RR experiment at a potential of − 0.5 V, where the maximum product formation was observed. Fig. 2e shows the overall current density and FEs of C_2H_5OH and CH_3OH formation during the long-term experiment. As shown in Fig. 2e, the MoP-Im exhibited a stable total current density of about − 90 mA/cm^2 at the potential of − 0.5 V with average FEs of about 60.1% and 9% for C_2H_5OH and CH_3OH during a 112-hour continuous process. The recorded total current density of the MoP-Im indicates less than 8% decay over the entire period. The stability results suggest that the presence of the Im stabilize the MoP-Im electrode in long-term eCO_2RR and prevent the catalysts leaching, which usually occurs in long-term processes (section S13, Supplementary Materials) [32].

3.3. Characterization of the catalyst layer

To gain more insight into the effect of the Im on the CO_2 diffusion in the catalyst layer and electron transfer properties of MoP-Im, we performed electrochemical impendence spectroscopy (EIS) experiments (section S14, Supplementary Materials). These experiments were performed at a potential of − 0.4 V where the activities of MoP-Im and MoP catalysts are limited by both diffusion of CO_2 as a reactant from bulk to the catalyst surface (linear region at low frequencies of the Nyquist plot) and the electron transfer from the surface of the catalyst to the reactant (semi-circle region at high frequencies of the Nyquist plot).[33–36] Fig. 3a shows the fitted EIS spectra of MoP-Im and MoP catalysts using the Randles circuit model. The EIS results from the kinetic-controlled region (semi-circle region) indicate a smaller charge transfer resistance (R_{ct}) for the MoP-Im (~10 ohms) compared to MoP (~12 ohms) suggesting improved electron transfer kinetics of the Mo atoms for the MoP-Im co-catalyst. This result is consistent with the XANES and XPS analyses, where we observed changes in electronic properties of the MoP-Im co-catalyst.[22] Moreover, we extracted the Warburg factors (σ_W) for MoP-Im and MoP catalysts from EIS results by plotting the gradient of the linear plot of the real impedance as a function of the reciprocal of the square root of the frequency at low-frequency range (diffusion-controlled region, section S14, Supplementary Materials). [33–36] Our results indicate Warburg factors of 10.35 and 15.85 Ω/s$^{1/2}$ for MoP-Im and MoP catalysts, respectively. The CO_2 diffusion coefficients (D_{CO2}) of MoP-Im and MoP catalysts were calculated using extracted Warburg factors (section S14, Supplementary Materials). The results illustrate about 20% higher D_{CO2} (5.31 ×10^{-11} m^2/s) of the MoP-Im than that of MoP (4.43 × 10^{-11} m^2/s) indicating a higher CO_2 diffusion rate from the bulk to the active sites of MoP-Im compared to the MoP (section S14, Supplementary Materials). This results in 1.8 times higher availability of CO_2 on the active sites of MoP-Im for the reaction. The EIS analysis confirms that the higher availability of CO_2 near the catalyst surface and the lower charge transfer resistance of Mo active sites enhance the activity of the MoP-Im compared to the MoP for C_2H_5OH production (section S9, Supplementary Materials). These results are consistent with our calculations, where about five times higher exchange current density and TOF_{C2H5OH} (intrinsic activity normalized per Mo active sites) were observed for the MoP-Im.

To further elucidate the effect of the Im on the catalyst layer, we obtained CO_2 adsorption isotherms for MoP-Im and MoP (section S15, Supplementary Materials). The CO_2 adsorption isotherms of the studied catalysts at 298 K are depicted in Fig. S20 (section S15, Supplementary Materials). These results indicate CO_2 adsorption of 228 μmol/g for MoP-Im at a relative pressure of 0.01656, which is about 34% higher than that of MoP (171 μmol/g), suggesting higher CO_2 uptake ability of MoP-Im compared with MoP. In addition, we conducted static and advancing contact angle measurements to study the wetting properties of MoP-Im and MoP catalysts (section S16, Supplementary Materials). The results shown in Fig. 3b-e indicate that the Im decreases the surface energy (*i.e.*, increases hydrophobicity) of the catalyst layer, which controls water content on the surface of MoP nanoparticles and suppresses the competing hydrogen evolution reaction for the MoP-Im (see Fig. S21 and Table S8, Supplementary Materials) [37].

3.4. Mechanistic understanding

We conducted *in-situ* Raman spectroscopy during eCO_2RR to gain an insight into the origin of a higher C_{2+} production activity of the MoP-Im (section S17, Supplementary Materials). The constructive Raman spectra at open circuit potential (OCP) shown in Fig. 4 confirm the stability of the synthesized catalysts under experimental conditions. Fig. 4 indicates five distinct Raman peaks of 290, 380, 1063, 1520, and 2160 cm^{-1} at the cathodic potential of − 0.5 V where 1063 and 1520 cm^{-}

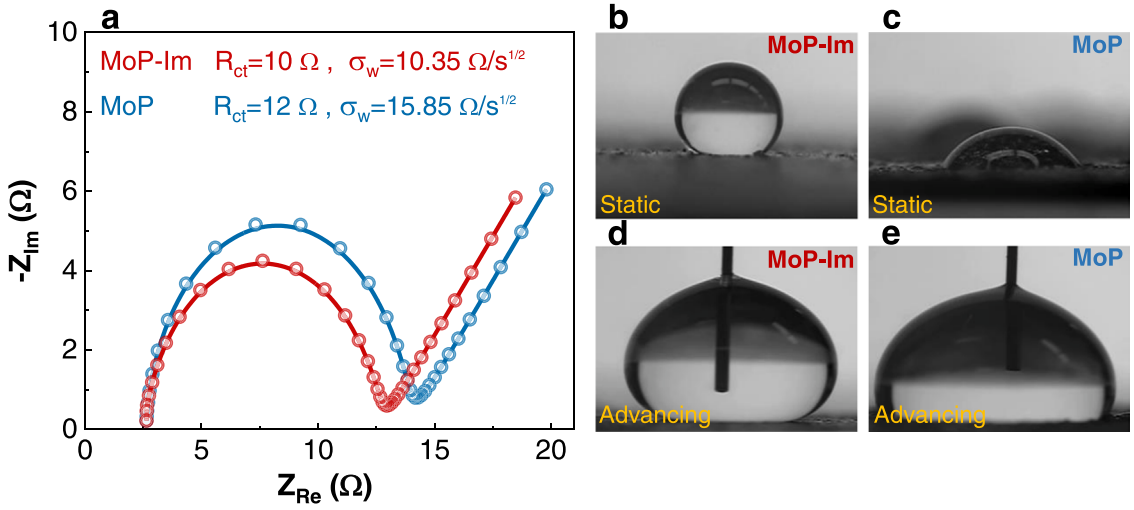

Fig. 3. Catalyst layer analyses of MoP-Im and MoP. (a) EIS experiments of MoP-Im and MoP catalysts. The experiments were conducted at a potential of − 0.4 V. The results indicate Warburg factors of 10.35 and 15.85 Ω/s$^{1/2}$ for MoP-Im and MoP, respectively. **(b,c)** Static and **(d,e)** Advancing contact angle analysis imageson MoP-Im and MoP electrodes with the hybrid electrolytes (3 M KOH, 3 M KCl). The wettability analysis reveals the hydrophobic character of MoP-Im, as compared to the hydrophilic property of MoP. The diameter of the capillary tube was 100 microns.

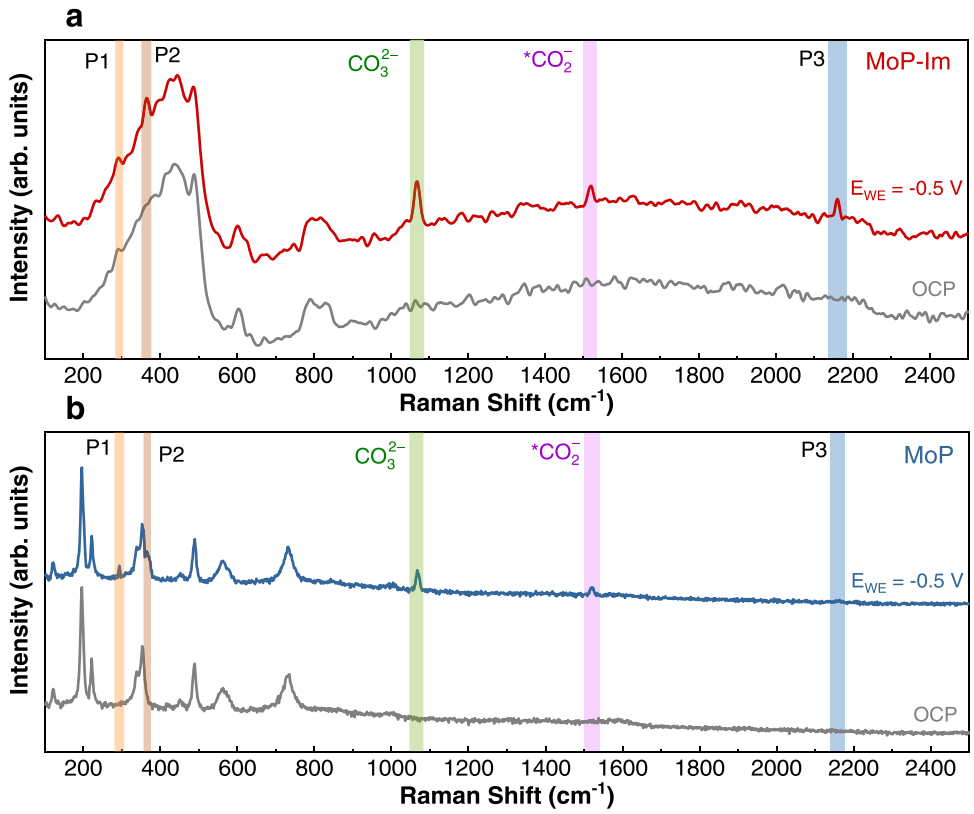

Fig. 4. *In-situ* electrochemical Raman spectroscopy experiments in eCO_2RR at open circuit potential (OCP) and applied cathodic potential of − 0.5 V. (a) *In-situ* Raman spectra of MoP-Im electrode, and (b) pristine MoP electrode under identical experimental conditions.

[1] peaks are attributed to the carbonate (CO_3^{2-}) and adsorbed carboxylate ($*CO_2^-$) species [38,39]. Our peak analysis shows that the concentration of CO_3^{2-} representing CO_2 molecules in the aqueous electrolytes (Raman peak at 1063 cm^{-1}) on the surface of the MoP-Im is about 30% higher at a potential of − 0.5 V than on MoP (section S17, Supplementary Materials); this is consistent with our diffusion coefficient calculation and CO_2 isotherm results (sections S14 and S15, Supplementary Materials). This clearly shows that the higher CO_2 diffusion affinity of the MoP-Im catalyst leads to higher local concentrations of CO_3^{2-}, and thus suggests a higher overall activity of the MoP-Im in eCO_2RR. Similarly, Fig. 4 shows about 50% higher concentration of $*CO_2^-$ (Raman peak at 1520 cm^{-1}) at the surface of the MoP-Im compared to MoP at a potential of − 0.5 V. Comparing these results, we found that the changes in the local concentration of $*CO_2^-$ are much larger than those observed for CO_3^{2-}. These results suggest that the Im enhances the diffusion of the reactant toward the catalyst surface and, more importantly, increases the number of stabilized $*CO_2^-$ intermediates on the MoP-Im surface (sections S14 and S15, Supplementary Materials). Our DFT calculations also confirm that the imidazolium in Im structure can bind on MoP(100) and MoP(001) surfaces with N atoms on Mo top sites and facilitate the charge transfer to the adsorbed CO_2 species. This results in increasing the CO_2 binding strength on the surface Mo-atoms of MoP-Im (section S18, Supplementary Materials).

To gain more insight about a higher C-C coupling and ethanol production rates of MoP-Im, we further investigated the differences between three Raman peaks centered at 290, 380, and 2160 cm^{-1} which are correlated to the restricted rotation of adsorbed *CO (P1), Mo-CO stretching (P2), and *C-O stretching (P3), respectively [27,40,41]. It is worth noting that as a metal surface adsorbs *CO intermediates, the electrons are partially transferred from d-orbitals of the metal atoms on to anti-bonding molecular orbitals of *CO intermediates [40,41]. This electron-transfer strengthens the Mo-CO bond and increases of the vibrational frequencies for the Mo-CO bond [27]. Therefore, higher Mo-CO stretching peak (P2) is attributed to the strength of the Mo-CO bond.

Our peak analysis shows that the intensity of the P2 peak for MoP-Im is higher than that of MoP catalyst, and P2/P1 ratio for MoP-Im catalyst at the potential − 0.5 V (P2/P1 ≅ 1.47) is about 47% higher than that of MoP catalyst (P2/P1 ≅ 1). The higher P2/P1 ratio for MoP-Im indicates that the *CO intermediates are stabilized on the surface of MoP-Im which results in higher C-C coupling [40,41]. This is consistent with previous studies where it has been confirmed that the intensity ratio of P1 and P2 peaks are potential dependent and higher P2/P1 Raman peak ratios are linked to a higher C-C coupling and C_{2+} products formation [40]. Furthermore, our *in-situ* Raman spectroscopy results show a higher intensity P3 (*C-O stretching) peak of MoP-Im compared to MoP catalyst at the potential of − 0.5 V indicating a high concentration/coverage of adsorbed *CO intermediates on the surface of MoP-Im. These results reveal that the high number of adsorbed *CO intermediates on the surface and the higher binding strength of *CO intermediates on the Mo atoms in presence of the Im are the main reasons for a greater C-C coupling and thereby a higher C_2H_5OH production for MoP-Im compared to MoP catalyst [41].

4. Conclusions

In summary, we have synthesized and tested the electrocatalytic performance of the MoP-Im co-catalyst for CO_2RR in a hybrid electrolyte of 3 M KOH and 3 M KCl. Physicochemical characterizations, such as XPS, XANES, and TEM experiments and electrochemical analyses, such as Tafel plot and EIS studies, suggested that the Im works together with MoP nanoparticles to produce C_2H_5OH by increasing CO_2-to-water ratio at the catalyst layer due to high CO_2 diffusion and hydrophobic properties of the ionomer and alters the electronic properties of the Mo atoms at the surface of the catalyst. I*n-situ* Raman spectroscopy confirmed that the imidazolium layer not only increases the number of CO_2 molecules

near the catalyst surface but also stabilizes adsorbed $*CO_2^-$ and *CO intermediates at the surface of catalyst that promotes C-C coupling and C_2H_5OH formation activity of MoP-Im. Moreover, DFT calculations suggest that the Im can increase the CO_2 binding strength and charge transfer to accelerate the reaction. The demonstrated electrocatalytic process using the TMP class of catalysts and imidazolium-based ionomer in this study suggests a promising approach for lowering eCO_2RR barriers toward high rate C_2^+ production in a sustainable fashion.

CRediT authorship contribution statement

Mohammad Asadi and Mohammadreza Esmaeilirad conceived the idea of the work. Mohammadreza Esmaeilirad synthesized the nanostructured materials. Mohammadreza Esmaeilirad, Alireza Kondori and Ahmad M. Harzandi performed electrochemical experiments and data analyses. Mohammadreza Esmaeilirad and Carlo U. Segre did the XRD characterization and analysis. Mohammadreza Esmaeilirad and Alireza Kondori did the XPS, Raman, FTIR and NMR characterizations. Carlo U. Segre conducted the XAS analysis. Mahmoud Tamadoni Saray and Reza Shahbazian-Yassar performed the SEM and TEM characterizations. Sreya Sarkar performed the contact angle analysis and was supervised by Constantine M. Megaridis. Nannan Shan and Larry A. Curtiss conducted DFT calculations. Mohammad Asadi supervised the experimental efforts in design, synthesis, characterization, and electrochemical testing and analyses. All authors discussed the results and assisted with manuscript preparation and revisions.

Declaration of Competing Interest

The authors declare that they have no known competing financial interests or personal relationships that could have appeared to influence the work reported in this paper.

Data availability

Data will be made available on request.

Acknowledgments

Mohammad Asadi's work was supported by National Science Foundation (NSF) Catalysis (Award No. CBET- 2135173) and Advanced Research Projects Agency-Energy (ARPA-E), United States (U.S.) Department of Energy (Award No. DE-AR0001581). We acknowledge the Northwestern University's Atomic and Nanoscale Characterization Experimental Center , which has received support from the Materials Research Science and Engineering Centers (MRSEC) program (Award No. DMR-1121262) at the Materials Research Center; the Nanoscale Science and Engineering Center (Award No. EEC−0647560) at the International Institute for Nanotechnology; and the State of Illinois, through the International Institute for Nanotechnology. Reza Shahbazian-Yassar efforts were supported by NSF (Award No. DMR-1809439). This work made use of instruments in the Electron Microscopy Service (Research Resources Center, University of Illinois at Chicago). The acquisition of the UIC JEOL JEM-ARM200CF was supported by the Major Research Instrumentation Program (MRI-R2) grant from the National Science Foundation (Award No. DMR-0959470). Nannan Shan and Larry A. Curtiss acknowledge the support from the Office of Science, Basic Energy Sciences, Materials Sciences and Engineering Division. The Materials Research Collaborative Access Team (MRCAT) operations are supported by the U.S. Department of Energy and the MRCAT member institutions. This research used resources of the Advanced Photon Source; a U.S. Department of Energy (DOE) Office of Science User Facility operated for the DOE Office of Science by Argonne National Laboratory. All research at Argonne National Laboratory, a U. S. Department of Energy Office of Science laboratory, operated by UChicago Argonne, LLC was conducted under Contract No. DE-AC02–06CH11357. Use of computational resources from Argonne Laboratory Computing Resource Center is acknowledged

Appendix A. Supporting information

Supplementary data associated with this article can be found in the online version at doi:10.1016/j.apcatb.2022.121681.

References

[1] C. Hope, K. Schaefer, Economic impacts of carbon dioxide and methane released from thawing permafrost, Nat. Clim. Change 6 (2016) 56–59, https://doi.org/10.1038/nclimate2807.
[2] C.F. Shih, T. Zhang, J. Li, C. Bai, Powering the future with liquid sunshine, Joule 2 (2018) 1925–1949, https://doi.org/10.1016/j.joule.2018.08.016.
[3] M. Esmaeilirad, A. Kondori, B. Song, A. Ruiz Belmonte, J. Wei, K. Kucuk, S. M. Khanvilkar, E. Efimoff, W. Chen, C.U. Segre, R. Shahbazian-Yassar, M. Asadi, Oxygen functionalized copper nanoparticles for solar-driven conversion of carbon dioxide to methane, ACS Nano 14 (2020) 2099–2108, https://doi.org/10.1021/acsnano.9b08792.
[4] M. Asadi, K. Kim, C. Liu, A.V. Addepalli, P. Abbasi, P. Yasaei, P. Phillips, A. Behranginia, J.M. Cerrato, R. Haasch, P. Zapol, B. Kumar, R.F. Klie, J. Abiade, L. a. Curtiss, A. Salehi-Khojin, Nanostructured transition metal dichalcogenide electrocatalysts for CO_2 reduction in ionic liquid, Science 353 (2016) (1979) 467–470, https://doi.org/10.1126/science.aaf4767.
[5] B.A. Rosen, A. Salehi-Khojin, M.R. Thorson, W. Zhu, D.T. Whipple, P.J.A. a Kenis, R.I. Masel, Ionic liquid-mediated selective conversion of CO_2 to CO at low overpotentials, Science 334 (2011) (1979) 643–644, https://doi.org/10.1126/science.1209786.
[6] H. Zhong, Y. Su, X. Chen, X. Li, R. Wang, Imidazolium- and triazine-based porous organic polymers for heterogeneous catalytic conversion of CO_2 into cyclic carbonates, ChemSusChem 10 (2017) 4855–4863, https://doi.org/10.1002/cssc.201701821.
[7] B.A. Rosen, J.L. Haan, P. Mukherjee, B. Braunschweig, W. Zhu, A. Salehi-Khojin, D. D. Dlott, R.I. Masel, In situ spectroscopic examination of a low overpotential pathway for carbon dioxide conversion to carbon monoxide, J. Phys. Chem. C. 116 (2012) 15307–15312, https://doi.org/10.1021/jp210542v.
[8] D.V. Vasilyev, P.J. Dyson, The role of organic promoters in the electroreduction of carbon dioxide, ACS Catal. 11 (2021) 1392–1405, https://doi.org/10.1021/acscatal.0c04283.
[9] K.U.D. Calvinho, A.B. Laursen, K.M.K. Yap, T.A. Goetjen, S. Hwang, N. Murali, B. Mejia-Sosa, A. Lubarski, K.M. Teeluck, E.S. Hall, E. Garfunkel, M. Greenblatt, G. C. Dismukes, Selective CO_2 reduction to C3 and C4 oxyhydrocarbons on nickel phosphides at overpotentials as low as 10 mV, Energy Environ. Sci. 11 (2018) 2550–2559, https://doi.org/10.1039/c8ee00936h.
[10] K.U.D. Calvinho, A.B. Laursen, K.M.K. Yap, T.A. Goetjen, S. Hwang, N. Murali, B. Mejia-Sosa, A. Lubarski, K.M. Teeluck, E.S. Hall, E. Garfunkel, M. Greenblatt, G. C. Dismukes, Selective CO_2 reduction to C3 and C4 oxyhydrocarbons on nickel phosphides at overpotentials as low as 10 mV, Energy Environ. Sci. 11 (2018) 2550–2559, https://doi.org/10.1039/c8ee00936h.
[11] L. Ji, L. Li, X. Ji, Y. Zhang, S. Mou, T. Wu, Q. Liu, B. Li, X. Zhu, Y. Luo, X. Shi, A. M. Asiri, X. Sun, Highly Selective Electrochemical Reduction of CO_2 to Alcohols on an FeP Nanoarray, Angew. Chem. - Int. Ed. 59 (2020) 758–762, https://doi.org/10.1002/anie.201912836.
[12] L. Ji, L. Chang, Y. Zhang, S. Mou, T. Wang, Y. Luo, Z. Wang, X. Sun, Electrocatalytic CO_2 Reduction to Alcohols with High Selectivity over a Two-Dimensional Fe2P2S6 Nanosheet, ACS Catal. 9 (2019) 9721–9725, https://doi.org/10.1021/acscatal.9b03180.
[13] A. Kondori, M. Esmaeilirad, A. Baskin, B. Song, J. Wei, W. Chen, C.U. Segre, R. Shahbazian-Yassar, D. Prendergast, M. Asadi, Identifying Catalytic Active Sites of Trimolybdenum Phosphide (Mo3P) for Electrochemical Hydrogen Evolution, Adv. Energy Mater. 9 (2019) 1–9, https://doi.org/10.1002/aenm.201900516.
[14] R. Liu, Y. Dai, J. Li, X. Chen, C. Pan, J. Yang, Q. Li, 1-(3-Aminopropyl)imidazole functionalized poly(vinyl chloride) for high temperature proton exchange membrane fuel cell applications, J. Membr. Sci. 620 (2021), 118873, https://doi.org/10.1016/j.memsci.2020.118873.
[15] D. Huang, Y. Ding, H. Jiang, S. Sun, Z. Ma, K. Zhang, L. Pan, Y. Li, Functionalized Elastomeric Ionomers Used as Effective Toughening Agents for Poly(lactic acid): Enhancement in Interfacial Adhesion and Mechanical Performance, ACS Sustain. Chem. Eng. 8 (2020) 573–585, https://doi.org/10.1021/acssuschemeng.9b06123.
[16] C. United, S.L.M.P. Lawrence, Berkeley National Lab. (LBNL), Berkeley, Mater. Data MoP Mater. Proj. (2020), https://doi.org/10.17188/1197238.
[17] Y. Huang, J. Ge, J. Hu, J. Zhang, J. Hao, Y. Wei, Nitrogen-Doped Porous Molybdenum Carbide and Phosphide Hybrids on a Carbon Matrix as Highly Effective Electrocatalysts for the Hydrogen Evolution Reaction, Adv. Energy Mater. 8 (2018) 1701601, https://doi.org/10.1002/aenm.201701601.
[18] Y. Zhang, G. Chen, L. Wu, K. Liu, H. Zhong, Z. Long, M. Tong, Z. Yang, S. Dai, Two-in-one: construction of hydroxyl and imidazolium-bifunctionalized ionic networks in one-pot toward synergistic catalytic CO_2 fixation, Chem. Commun. 56 (2020) 3309–3312, https://doi.org/10.1039/C9CC09643D.
[19] M.S. Duyar, A. Gallo, S.K. Regli, J.L. Snider, J.A. Singh, E. Valle, J. McEnaney, S. F. Bent, M. Rønning, T.F. Jaramillo, Understanding selectivity in co2

hydrogenation to methanol for mop nanoparticle catalysts using in situ techniques, Catalysts 11 (2021) 1–18, https://doi.org/10.3390/catal11010143.
[20] W. Ren, X. Tan, X. Chen, G. Zhang, K. Zhao, W. Yang, C. Jia, Y. Zhao, S.C. Smith, C. Zhao, Confinement of Ionic Liquids at Single-Ni-Sites Boost Electroreduction of CO_2 in Aqueous Electrolytes, ACS Catal. 10 (2020) 13171–13178, https://doi.org/10.1021/acscatal.0c03873.
[21] A.S. Varela, W. Ju, T. Reier, P. Strasser, Tuning the Catalytic Activity and Selectivity of Cu for CO_2 Electroreduction in the Presence of Halides, ACS Catal. 6 (2016) 2136–2144, https://doi.org/10.1021/acscatal.5b02550.
[22] M. Esmaeilirad, A. Baskin, A. Kondori, A. Sanz-Matias, J. Qian, B. Song, M. Tamadoni Saray, K. Kucuk, A.R. Belmonte, P.N.M. Delgado, J. Park, R. Azari, C. U. Segre, R. Shahbazian-Yassar, D. Prendergast, M. Asadi, Gold-like activity copper-like selectivity of heteroatomic transition metal carbides for electrocatalytic carbon dioxide reduction reaction, Nat. Commun. 12 (2021) 5067, https://doi.org/10.1038/s41467-021-25295-y.
[23] S. Mou, T. Wu, J. Xie, Y. Zhang, L. Ji, H. Huang, T. Wang, Y. Luo, X. Xiong, B. Tang, X. Sun, Boron Phosphide Nanoparticles: A Nonmetal Catalyst for High-Selectivity Electrochemical Reduction of CO_2 to CH3OH, Adv. Mater. 31 (2019), https://doi.org/10.1002/adma.201903499.
[24] H. Xu, D. Rebollar, H. He, L. Chong, Y. Liu, C. Liu, C.-J. Sun, T. Li, J.V. Muntean, R. E. Winans, D.-J. Liu, T. Xu, Highly selective electrocatalytic CO_2 reduction to ethanol by metallic clusters dynamically formed from atomically dispersed copper, Nat. Energy 5 (2020) 623–632, https://doi.org/10.1038/s41560-020-0666-x.
[25] X. Wang, Z. Wang, F.P. García de Arquer, C.T. Dinh, A. Ozden, Y.C. Li, D.H. Nam, J. Li, Y.S. Liu, J. Wicks, Z. Chen, M. Chi, B. Chen, Y. Wang, J. Tam, J.Y. Howe, A. Proppe, P. Todorović, F. Li, T.T. Zhuang, C.M. Gabardo, A.R. Kirmani, C. McCallum, S.F. Hung, Y. Lum, M. Luo, Y. Min, A. Xu, C.P. O'Brien, B. Stephen, B. Sun, A.H. Ip, L.J. Richter, S.O. Kelley, D. Sinton, E.H. Sargent, Efficient electrically powered CO_2-to-ethanol via suppression of deoxygenation, Nat. Energy 5 (2020) 478–486, https://doi.org/10.1038/s41560-020-0607-8.
[26] M. Luo, Z. Wang, Y.C. Li, J. Li, F. Li, Y. Lum, D.-H. Nam, B. Chen, J. Wicks, A. Xu, T. Zhuang, W.R. Leow, X. Wang, C.-T. Dinh, Y. Wang, Y. Wang, D. Sinton, E. H. Sargent, Hydroxide promotes carbon dioxide electroreduction to ethanol on copper via tuning of adsorbed hydrogen, Nat. Commun. 10 (2019) 5814, https://doi.org/10.1038/s41467-019-13833-8.
[27] Y.C. Li, Z. Wang, T. Yuan, D.H. Nam, M. Luo, J. Wicks, B. Chen, J. Li, F. Li, F.P. G. de Arquer, Y. Wang, C.T. Dinh, O. Voznyy, D. Sinton, E.H. Sargent, Binding Site Diversity Promotes CO_2 Electroreduction to Ethanol, J. Am. Chem. Soc. 141 (2019) 8584–8591, https://doi.org/10.1021/jacs.9b02945.
[28] W. Ma, S. Xie, T. Liu, Q. Fan, J. Ye, F. Sun, Z. Jiang, Q. Zhang, J. Cheng, Y. Wang, Electrocatalytic reduction of CO_2 to ethylene and ethanol through hydrogen-assisted C–C coupling over fluorine-modified copper, Nat. Catal. 3 (2020) 478–487, https://doi.org/10.1038/s41929-020-0450-0.
[29] T.-T. Zhuang, Z.-Q. Liang, A. Seifitokaldani, Y. Li, P. De Luna, T. Burdyny, F. Che, F. Meng, Y. Min, R. Quintero-Bermudez, C.T. Dinh, Y. Pang, M. Zhong, B. Zhang, J. Li, P.-N. Chen, X.-L. Zheng, H. Liang, W.-N. Ge, B.-J. Ye, D. Sinton, S.-H. Yu, E. H. Sargent, Steering post-C–C coupling selectivity enables high efficiency electroreduction of carbon dioxide to multi-carbon alcohols, Nat. Catal. 1 (2018) 421–428, https://doi.org/10.1038/s41929-018-0084-7.
[30] D. Karapinar, N.T. Huan, N. Ranjbar Sahraie, J. Li, D. Wakerley, N. Touati, S. Zanna, D. Taverna, L.H. Galvão Tizei, A. Zitolo, F. Jaouen, V. Mougel, M. Fontecave, Electroreduction of CO_2 on Single-Site Copper-Nitrogen-Doped Carbon Material: Selective Formation of Ethanol and Reversible Restructuration of the Metal Sites, Angew. Chem. Int. Ed. 58 (2019) 15098–15103, https://doi.org/10.1002/anie.201907994.
[31] J. Yang, A.R. Mohmad, Y. Wang, R. Fullon, X. Song, F. Zhao, I. Bozkurt, M. Augustin, E.J.G. Santos, H.S. Shin, W. Zhang, D. Voiry, H.Y. Jeong, M. Chhowalla, Ultrahigh-current-density niobium disulfide catalysts for hydrogen evolution, Nat. Mater. 18 (2019) 1309–1314, https://doi.org/10.1038/s41563-019-0463-8.
[32] M. Koy, P. Bellotti, M. Das, F. Glorius, N-Heterocyclic carbenes as tunable ligands for catalytic metal surfaces, Nat. Catal. 4 (2021) 352–363, https://doi.org/10.1038/s41929-021-00607-z.
[33] G. Barbero, Theoretical interpretation of Warburg's impedance in unsupported electrolytic cells, Phys. Chem. Chem. Phys. 19 (2017) 32575–32579, https://doi.org/10.1039/C7CP07101A.
[34] A. Husain, K. Kupwade-Patil, A.F. Al-Aibani, M.F. Abdulsalam, In situ electrochemical impedance characterization of cement paste with volcanic ash to examine early stage of hydration, Constr. Build. Mater. 133 (2017) 107–117, https://doi.org/10.1016/j.conbuildmat.2016.12.054.
[35] T.Q. Nguyen, C. Breitkopf, Determination of Diffusion Coefficients Using Impedance Spectroscopy Data, J. Electrochem. Soc. 165 (2018) E826–E831, https://doi.org/10.1149/2.1151814jes.
[36] V. Grozovski, S. Vesztergom, G.G. Láng, P. Broekmann, Electrochemical hydrogen evolution: H+ or H2O reduction? A rotating disk electrode study, J. Electrochem. Soc. 164 (2017) E3171–E3178, https://doi.org/10.1149/2.0191711jes.
[37] C. Kim, J.C. Bui, X. Luo, J.K. Cooper, A. Kusoglu, A.Z. Weber, A.T. Bell, Tailored catalyst microenvironments for CO_2 electroreduction to multicarbon products on copper using bilayer ionomer coatings, Nat. Energy 6 (2021) 1026–1034, https://doi.org/10.1038/s41560-021-00920-8.
[38] X. Chen, J. Chen, N.M. Alghoraibi, D.A. Henckel, R. Zhang, U.O. Nwabara, K. E. Madsen, P.J.A. Kenis, S.C. Zimmerman, A.A. Gewirth, Electrochemical CO_2-to-ethylene conversion on polyamine-incorporated Cu electrodes, Nature, Catalysis 4 (2021) 20–27, https://doi.org/10.1038/s41929-020-00547-0.
[39] I. v Chernyshova, P. Somasundaran, S. Ponnurangam, On the origin of the elusive first intermediate of CO_2 electroreduction, Proc. Natl. Acad. Sci. 115 (2018) E9261–E9270, https://doi.org/10.1073/pnas.1802256115.
[40] C. Zhan, F. Dattila, C. Rettenmaier, A. Bergmann, S. Kühl, R. García-Muelas, N. López, B.R. Cuenya, Revealing the CO Coverage-Driven C–C Coupling Mechanism for Electrochemical CO_2 Reduction on Cu2O Nanocubes via Operando Raman Spectroscopy, ACS Catal. 11 (2021) 7694–7701, https://doi.org/10.1021/acscatal.1c01478.
[41] H. An, L. Wu, L.D.B. Mandemaker, S. Yang, J. de Ruiter, J.H.J. Wijten, J.C. L. Janssens, T. Hartman, W. van der Stam, B.M. Weckhuysen, Sub-second time-resolved surface-enhanced raman spectroscopy reveals dynamic CO intermediates during electrochemical CO_2 reduction on copper, Angew. Chem. Int. Ed. 60 (2021) 16576–16584, https://doi.org/10.1002/anie.202104114.